Ultrafast phonon diffuse scattering as a tool for observing chiral phonons in monolayer hexagonal lattices

Tristan L. Britt [1,*] and Bradley J. Siwick [1,2,†]

[1]*Department of Physics, Center for the Physics of Materials, McGill University,*
3600 rue Université, Montréal, Québec H3A 2T8, Canada
[2]*Department of Chemistry, McGill University, 801 rue Sherbrooke Ouest, Montréal, Québec H3A 0B8, Canada*

At the 2D limit, hexagonal systems such as monolayer transition metal dichalcogenides (TMDs) and graphene exhibit unique coupled spin and momentum-valley physics (valley pseudospin) owing to broken spatial inversion symmetry and strong spin-orbit coupling. Circularly polarized light provides the means for pseudospin-selective excitation of excitons (or electrons and holes) and can yield momentum-valley polarized populations of carriers that are the subject of proposed valleytronic applications. The chirality of these excited carriers has important consequences for the available relaxation/scattering pathways, which must conserve (pseudo)angular momentum as well as energy. One available relaxation channel that satisfies these constraints is coupling to chiral phonons. Here, we show that chiral carrier-phonon coupling following valley-polarized photoexcitation is expected to lead to a strongly valley-polarized chiral phonon distribution when this relaxation mechanism is dominant. This momentum valley phonon polarization is directly measurable using ultrafast phonon diffuse scattering techniques. Using *ab initio* calculations, we show how the dynamic phonon occupations and valley anisotropy determined by nonequilibrium observations can provide a new window on the physical processes that drive carrier valley depolarization in monolayer TMDs.

I. INTRODUCTION

2D Transition-metal dichalcogenides (TMDs) are currently the subject of intense research due to their exciting electronic and optoelectronic properties. These arise from the highly correlated nature of their spin [1,2], valley [3,4], electronic [5], and vibrational [6] degrees of freedom which can vary dramatically with the number of layers, most notably with the breaking of spatial inversion symmetry in monolayers. In systems that additionally feature strong spin-orbit coupling [7–9] (SOC) such as monolayer (1L) molybdenum disulfide (MoS$_2$) or tungsten diselenide (WSe$_2$), the coupled spin and momentum-valley physics further [10] allow for direct control over these degrees of freedom [3,11] using circularly polarized light. Photoexcitation can be used to generate electron hole pairs in either the K or K' region of the Brillouin zone (BZ), where the carriers have opposite orbital angular momentum. The selective excitation of carriers in terms of both orbital (angular) and valley momentum has been termed carrier valley polarization.

From the perspective of the phonons, hexagonal lattices also exhibit unusual features not found in other space groups. Typically, phonon normal modes in single crystal systems feature phase mismatched linearly polarized atomic displacements. At the K points of a 2D hexagonal lattice, however, three-fold symmetry results in the atomic displacements associated with certain optical and acoustic phonon modes executing circular orbits. In bulk (layered) hexagonal materials, these left and right circularly polarized K-point phonons tend to be degenerate and do not carry net angular momentum since the basis atoms tend to orbit in opposite directions. However, in monolayer TMDs, the presence of strong SOC and broken inversion symmetry lifts the degeneracy of circular polarized phonons near K and K', and yields chiral phonon modes with nonzero pseudo angular momentum (PAM). These chiral phonons posses finite Berry curvature and can induce a phonon Hall effect, making them prime candidates in unraveling the origins of the thermal Hall effect in many quantum systems, such as Kitaev spin liquids (e.g., $\alpha - \text{RuCl}_3$ [12]), cuprate superconductors [13], spin ices [14], and frustrated magnets [15].

Taken together, these unusual features of the carriers and phonons near K (K') points can be expected to yield unusual handedness to the electron-phonon coupling (EPC) interaction in monolayer TMDs. Specifically, during the relaxation of an initially valley-polarized (hot) charge carrier distribution, the equilibration of valley polarized carriers involve intervalley ($K - K'$) transitions that require a change of orbital-angular momentum and raise questions about angular momentum conservation. One intervalley relaxation channel that conserves both angular momentum and energy is chiral electron-phonon scattering. Such interactions are thought to be an important factor in the process of valley depolarization. Here we propose an experimental procedure for direct observation of the nonequilibrium time- and momentum-dependent chiral phonon formation involved in phonon-assisted valley

*tristan.britt@mail.mcgill.ca
†bradley.siwick@mcgill.ca

depolarization. The approach proposed is based on ultra-fast electron [16] or x-ray techniques that measure the time-dependence of phonon diffuse scattering following optical excitation [17,18] rather than the time-evolution of Bragg-peak intensities. These rapidly maturing approaches have already found application to many phenomena that emerge from momentum dependent electron-phonon interactions, such as inelastic electron-phonon scattering [19–22], soft phonon-modes [23], and polaron formation [24] in materials. While indirect methods have been proposed to observe chiral phonons via their signature in the thermal Hall effect [25], and the observation of chiral phonons have been reported [26] via circular dichroism in the optical transmission of the material, such methods do not directly measure chiral phonon emission. The hallmark of chiral phonon emission during carrier valley depolarization is the generation of a momentum-valley polarized phonon distribution. The direct measurement of such a transient phonon distribution during carrier-valley depolarization in 1L-MoS$_2$ using ultrafast diffuse scattering is the focus of this work. Overall, the goal is to build on the recent ultrafast electron diffuse scattering (UEDS) study of 1L-MoS$_2$ [27] and open a window on chiral phonon generation.

This paper is organized as follows. First, we discuss the relevant symmetries of hexagonal lattices, creating assignments for the orbitals relevant to intervalley photo-carrier relaxation. Next, we illustrate that spin-conserving, intervalley momentum (and energy) relaxation channels for charge carriers involve a change in orbital angular momentum (OAM), which can be provided by carrier-chiral phonon scattering in monolayer hexagonal lattices. Finally, we propose an ultrafast direct detection method for chiral phonons in circular polarized pump-phonon diffuse scattering probe experiments, which report on the expected momentum-valley polarized, chiral phonon distribution that can be generated following optical excitation.

II. SPIN AND VALLEY CHARGE CARRIER PHYSICS

It has been long known [28] that at the K point in TMDs of chemical formulas MX_2, the valence band is dominated by the $|d_{x^2-y^2}\rangle$ and $|d_{xy}\rangle$ (E symmetry) orbitals on M (with small contribution from $|p_x\rangle$ and $|p_y\rangle$ on X) while the conduction band is primarily $|d_{z^2}\rangle$ (A_1 symmetry) on M. The valence hybridization at the valley is given by

$$|\Psi_v\rangle = \frac{1}{\sqrt{2}}(|d_{x^2-y^2}\rangle + i\tau |d_{xy}\rangle) \quad (1)$$

where these combinations are the only allowed owing to the C_{3h} point group symmetry of the hexagonal lattice. Application of the prime generator of this point group at the valleys, namely threefold rotation symmetry about the out-of-plane (parallel to the **c** crystal axis) $\mathcal{R}\{2\pi/3, \hat{z}\}$, allows for determination of the azimuthal quantum numbers ℓ in the valence and conduction bands. By defining a valley index $\tau = \pm 1$ that denotes the K (K') valley, we find

$$\mathcal{R}\{2\pi/3, \hat{z}\}|\Psi_v^\tau\rangle = |\Psi_v^\tau\rangle = e^{i\ell_v 2\pi/3}|\Psi_v^\tau\rangle \Rightarrow \ell_v = 0, \quad (2a)$$

$$\mathcal{R}\{2\pi/3, \hat{z}\}|\Psi_c^\tau\rangle = e^{i\tau 2\pi/3}|\Psi_c^\tau\rangle = e^{i\ell_c 2\pi/3}|\Psi_c^\tau\rangle \Rightarrow \ell_c = \tau \quad (2b)$$

showing that intravalley interband transitions are allowed so long as they obey the selection rule $\ell_c - \ell_v = \tau = \ell_{\text{photon}}$.

To see that it is possible to directly control the valley and spin indices of the charge carrier simultaneously requires ascribing a Hamiltonian to this system. To completely capture the necessary physics in 2D TMDs requires a full seven-band model [29–31]. Yet, Lowdin partitioning [32] can be used to reduce the degrees of freedom to a basis set of two bands. This Hamiltonian, first derived by Xiao *et al.* [3,33], has contributions from **k** · **p** theory $\hat{\mathcal{H}}_{\mathbf{k}\cdot\mathbf{p}}$, and from the spin-orbit coupling $\hat{\mathcal{H}}_{\text{SO}}$:

$$\hat{\mathcal{H}} = \hat{\mathcal{H}}_{\mathbf{k}\cdot\mathbf{p}} + \hat{\mathcal{H}}_{\text{SO}}$$

$$= at(\tau k_x \hat{\sigma}_x + k_y \hat{\sigma}_y) + \frac{\Delta}{2}\hat{\sigma}_z - \tau \Delta_{\text{VB}} \frac{\hat{\sigma}_z - 1}{2}\hat{s}_z, \quad (3)$$

where $\hat{\mathbf{S}} = (\hat{s}_x, \hat{s}_y, \hat{s}_z)$ is the vector of spin Pauli matrices, $\hat{\sigma}_z$ is the Pauli matrix for the 2 basis functions [34], a the lattice constant, t the effective hopping integral, and Δ_{VB} the energetic spin splitting of the valence band. We can compute the degree to which circularly polarized photoexcitation couples to electronic transitions via the transition amplitudes of the interband momenta operators, namely,

$$P_\pm = P_x \pm iP_y, \quad (4a)$$

$$P_\alpha \equiv m_0 \left\langle u_c \left| \frac{1}{\hbar} \frac{\partial \hat{H}}{\partial k_\alpha} \right| u_v \right\rangle, \quad (4b)$$

where u is the periodic part of the Bloch wave function [29] in the valence (v) and conduction (c) bands. In terms of the spin-split band gap $\Delta' \equiv \Delta - \Delta_{\text{VB}}\tau s_z$, we can write these transition amplitudes as

$$|P_\pm(\mathbf{k})|^2 = \frac{m_0^2 a^2 t^2}{\hbar^2}\left(1 \pm \tau \frac{\Delta'}{\sqrt{\Delta'^2 + 4a^2 t^2 k^2}}\right)$$

$$\overset{\Delta' \gg atk}{=} \frac{m_0^2 a^2 t^2}{\hbar^2}(1 \pm \tau), \quad (5)$$

where *ab initio* calculations predict [7] that for TMDs, $\Delta' \gg atk$. Optical fields couple only to the orbital part of the wave function and spin is conserved in the optical transitions. We therefore obtain the following excitation rule; transitions of electrons to the conduction band (and creation of holes in the valence band) in a definite valley are allowed by photoexcitation of handedness τ (from the perspective of the sender) at energy at least Δ'. The stability of the electronic valley polarization has been verified experimentally in many different TMDs [3,35–37], where the photoexcitation will either generate an exciton (bound electron-hole pair) gas or electron-hole plasma, according to the photoinduced charge carrier density n_0.

2D hexagonal lattices fall in the C_{3h} point group [or point double group for spin-split band structure Fig. 1(a)], where the symmetry properties of the character table and corresponding allowed intra- and intervalley and band transitions have been well determined [11], see Table I. The valley depolarization of excitons at low density has previously been explained in 1L-MoS$_2$ [38,39] with reference to the electron-hole exchange interaction, not carrier-phonon interactions. With regards to impact ionization as a depolarization mechanism, even at n_0 as low as 10^{12} cm^{-2}, this carrier-carrier scattering has been
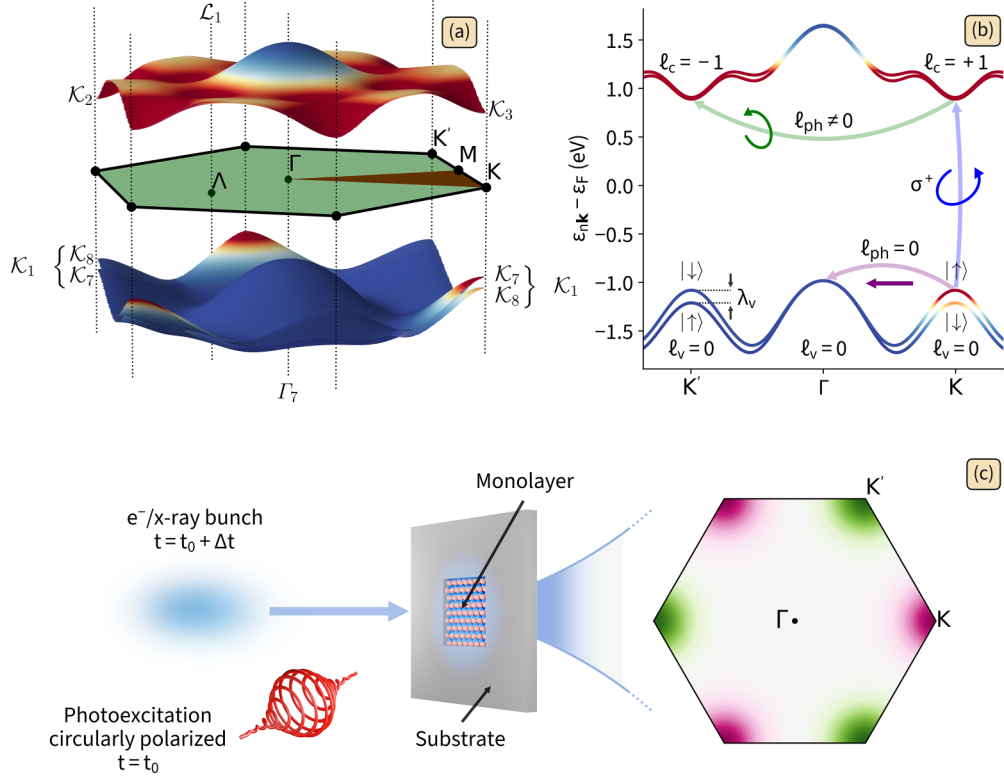
FIG. 1. PAM conserving intervalley carrier scattering and ultrafast phonon diffuse scattering measurements in 1L-MoS$_2$ (a) Spin-split valence and conduction band structure of 1L-MoS$_2$. The reducible BZ is shown in green and the irreducible BZ in red, with high symmetry points labeled. Calligraphic annotations denote the irreducible representations of the band structure at the corresponding high symmetry points for a given spin-split band. (b) Bands along the $K'\Gamma K$ direction with coloring identical to (a). Photoexcitation with right-circularly polarized light (blue arrow) leads to a valley-polarized charge carriers distribution around K. Left circularly polarized light drives excitation at K' (not shown). Spin and PAM conserving intervalley scattering processes for conduction (valence) band electrons (holes) to K' (Γ). Electron scattering must involve the emission of a chiral phonon (green arrow) and hole scattering can only involve nonchiral phonons (purple arrow). The valence band shows pronounced energy splitting of the spin states for monolayer TMDs ($\lambda_v \sim 100$ s of meV, much larger than even the highest-energy phonons). The equivalent splitting in the conduction band λ_c is much smaller (<10 s of meV, smaller than all K or K' phonons). (c) Schematic of the ultrafast diffuse scattering experiment. The sample is illuminated with circularly polarized light, after which the system is probed with an electron/x-ray bunch at a pump-probe delay time Δt. Diffuse scattering for a single representative BZ surrounding the Bragg peak at Γ is shown on the right. The colors of the K and K' regions match the arrow colors for the corresponding process illustrated in (b), allowing the separation of chiral electron scattering from nonchiral hole scattering.

shown to only redistribute excited electrons (holes) in the conduction (valence) band between K and K' after 10 ps (10 s of ns) [40]. More complicated carrier-carrier depo-

TABLE I. Spin-conserving selection rules based on the C_{3h} point group. The nature of the scattering process is given, well as an example of such a process in practice. The rule $(A \times B^*)^* = C$ should be read as a transition from electron momenta A to B requires a mediating phonon of momentum C.

	Selection Rule	Process
Intravalley:	$(\mathcal{K}_1 \times \mathcal{K}_1^*)^* = \Gamma_1$	Mainly hole relaxation
	$(\mathcal{L}_1 \times \mathcal{L}_1^*)^* = \Gamma_1$	Electron relaxation
	$(\Gamma_1 \times \Gamma_1^*)^* = \Gamma_1$	
Intervalley:	$(\mathcal{K}_3 \times \mathcal{K}_2^*)^* = \mathcal{K}_3$	Cond. electron scattering
	$(\mathcal{K}_1 \times \mathcal{K}_1^*)^* = \mathcal{K}_1$	Valence hole scattering
	$(\mathcal{L}_1 \times \mathcal{K}_3^*)^* = \mathcal{L}_1$	Hot carrier accumulation
	$(\Gamma_1 \times \mathcal{K}_1^*)^* = \mathcal{K}_1$	Carrier thermalization

larization mechanisms, as in the Dexter-like transport of momentum-separated excitons [41], become less relevant at large n_0 owing to the increased Coulombic screening of electrons and holes, and thus broken electron-hole correlations. Therefore, at n_0 greater than the exciton Mott threshold to an electron-hole plasma in monolayer TMDs [42–44], electron-phonon interactions are expected to be the dominant mechanism driving valley depolarization of the charge carrier distribution. Thus the measurements proposed here can, in principle, be used to monitor the transition from electron-phonon to exchange dominated valley depolarization.

The dominant intervalley (K to K') momentum (and energy) relaxation channels for K-valley polarized conduction band electrons, $(\mathcal{K}_3 \times \mathcal{K}_2^*)^* = \mathcal{K}_3$, are spin conserving, but require a change in the aziumthal quantum number ℓ, as shown in Fig. 1(b). This change in OAM can be provided by the emission or absorption of a chiral phonon at K' as we demonstrate in the next section. The equivalent process for holes requires a spin-flip, $(\mathcal{K}_8 \times \mathcal{K}_7^*)^* = \mathcal{K}_6$, due to the large valence band spin splitting and is expected to be much slower.

Spin-flip processes, such as the Bir-Aronov-Pikus mechanism [45] or Dyakonov-Pevel mechanism [46], occur on longer time scales.

The dominant intervalley (K to Γ) momentum (and energy) relaxation channels for K-valley polarized carriers involves valence hole scattering, $(\Gamma_1 \times \mathcal{K}_1^*)^* = \mathcal{K}_1$, and is allowed due to the spin and energy degeneracy at Γ as shown in Fig. 1(b). This channel can only involve scattering from nonchiral K phonons, since there is no associated change in OAM.

These details of hole scattering differ for selenide TMDs, where the valence band maxima at K and Γ are not closely spaced in energy like they are for the sulfide TMDs. In TMDs, it is also possible to exert some control over the relative valence energy at the Γ point by introducing strain.

It is worth mentioning that in these materials, previous computational [47] and experimental [48] work has shown that excited electrons primarily occupy states in the vicinity of the K and Λ valleys. These works further show that there is efficient scattering between them, $(\mathcal{L}_1 \times \mathcal{K}_3^*)^* = \mathcal{L}_1$, especially in the notable exception of WSe$_2$ where the Λ valley is energetically below K. This would result in an increase of phonon occupation at the sixfold degenerate Λ valleys. These works, however, use excitation energy well above the band gap such that charge carriers are occupied at Λ by the photoexcitation, which enables the efficient scattering to K. We can minimize the occupation of Λ phonons by selective photoexcitation resonant with the A exciton (band-gap excitation). Nonetheless, this scattering is momentum separated from the chiral K/K' scattering in momentum-resolved phonon diffuse scattering, meaning occupancy at Λ can be safely ignored in the discussion of chiral phonons.

III. PSEUDO ANGULAR MOMENTUM

To show that phonons in such a system can have $\ell_{\text{ph}} \neq 0$, we start by evaluating the angular momentum operator for the crystal. For a given atomic motion, we can determine its angular momentum (with respect to $\hat{z}$) as $\mathcal{J}_z = m\mathbf{r} \times \dot{\mathbf{r}}$, where $(\dot{\ }) \equiv \partial_t$. Defining the atomic displacement vector of all κth atoms in the pth unit cell as $\mathbf{u}_p = (u_{p1}^x \, u_{p1}^y \cdots u_{pn}^x \, u_{pn}^y)^T$, we can define the total angular momentum of the crystal as

$$\mathcal{J}_z = \sum_p m_\kappa \mathbf{u}_p \times \dot{\mathbf{u}}_p = \sum_{p\kappa} m_\kappa \left(u_{p\kappa}^x \dot{u}_{p\kappa}^y - \dot{u}_{p\kappa}^x u_{p\kappa}^y \right) = \sum_p \begin{pmatrix} u_{p1}^x \\ u_{p1}^y \\ \vdots \\ u_{pn}^x \\ u_{pn}^y \end{pmatrix}^T \begin{pmatrix} 0 & m_1 & & & \\ -m_1 & 0 & & & \\ & & \ddots & & \\ & & & 0 & m_n \\ & & & -m_n & 0 \end{pmatrix} \begin{pmatrix} \dot{u}_{p1}^x \\ \dot{u}_{p1}^y \\ \vdots \\ \dot{u}_{pn}^x \\ \dot{u}_{pn}^y \end{pmatrix} = \sum_p \mathbf{u}_p^T iM' \dot{\mathbf{u}}_p, \tag{6}$$

where $M' = \begin{pmatrix} 0 & i \\ i & 0 \end{pmatrix} \otimes \{m_\kappa\}$, $\{m_\kappa\}$ is the $n \times n$ diagonal matrix of atomic masses, and $\otimes$ is the Kronecker product. By defining $M = \begin{pmatrix} 0 & i \\ i & 0 \end{pmatrix} \otimes \mathbb{1}_{\mathbb{m}}$, we can apply second quantization to the atomic displacements in the normal mode coordinate formalism. These displacements can be written as

$$u_{p\kappa}^j = \sum_{\mathbf{q}\nu} \left(\varepsilon_{\mathbf{q}\nu}^\kappa \right)^j e^{i(\mathbf{R}_p \cdot \mathbf{q} - \omega_{\mathbf{q}\nu} t)} \sqrt{\frac{\hbar}{2\omega_{\mathbf{q}\nu} N m_\alpha}} a_{\mathbf{q}\nu} + \text{H.c.}, \tag{7}$$

where H.c. denotes the Hermitian conjugate, and $(\varepsilon_{\mathbf{q}\nu}^\kappa)^j$ the jth component of the atomic displacement of the κth atom at momentum $\mathbf{q}$ in mode ν at energy $\hbar\omega_{\mathbf{q}\nu}$, populated according to the creation operator $a_{\mathbf{q}\nu}^\dagger$. By ignoring terms like aa and $a^\dagger a^\dagger$ (which vary quickly and have no contribution in equilibrium), we express the total angular momentum in terms of these displacements as

$$\mathcal{J}_z = \frac{\hbar}{2N} \sum_p \sum_{\mathbf{q}\mathbf{q}'} \sum_{\nu\nu'} e^{i(\mathbf{q}'-\mathbf{q})\cdot\mathbf{R}_p} e^{i(\omega_{\mathbf{q}\nu} - \omega_{\mathbf{q}'\nu'})t} \times \left\{ \sqrt{\frac{\omega_{\mathbf{q}\nu}}{\omega_{\mathbf{q}'\nu'}}} \epsilon_{\mathbf{q}\nu}^\dagger M \epsilon_{\mathbf{q}'\nu'} a_{\mathbf{q}\nu}^\dagger a_{\mathbf{q}'\nu'} + \sqrt{\frac{\omega_{\mathbf{q}'\nu'}}{\omega_{\mathbf{q}\nu}}} \epsilon_{\mathbf{q}'\nu'}^T (-M) \epsilon_{\mathbf{q}\nu}^* a_{\mathbf{q}'\nu'} a_{\mathbf{q}\nu}^\dagger \right\}. \tag{8}$$

Noting further that $\epsilon_{\mathbf{q}'\nu'}^T(-M)\epsilon_{\mathbf{q}\nu}^* = \epsilon_{\mathbf{q}\nu}^\dagger M \epsilon_{\mathbf{q}'\nu'}$ and $\frac{1}{N}\sum_p e^{i(\mathbf{q}-\mathbf{q}')\cdot\mathbf{R}_p} = \delta_{\mathbf{q},\mathbf{q}'}$ and that the creation operators satisfy the commutation relation $[a_{\mathbf{q},\nu'}, a_{\mathbf{q},\nu}^\dagger] = \delta_{\nu'\nu}$, we can simplify this expression to obtain the nonequilibrium phonon angular momenta:

$$\mathcal{J}_z = \frac{\hbar}{2} \sum_{\mathbf{q}\mathbf{q}'} \sum_{\nu\nu'} \epsilon_{\mathbf{q}\nu}^\dagger M \epsilon_{\mathbf{q}'\nu'} a_{\mathbf{q}\nu}^\dagger a_{\mathbf{q}'\nu'} \left\{ \sqrt{\frac{\omega_{\mathbf{q}\nu}}{\omega_{\mathbf{q}'\nu'}}} + \sqrt{\frac{\omega_{\mathbf{q}'\nu'}}{\omega_{\mathbf{q}\nu}}} \right\}$$
$$\times \delta_{\mathbf{q},\mathbf{q}'} e^{i(\omega_{\mathbf{q}\nu} - \omega_{\mathbf{q}'\nu'})t} + \frac{\hbar}{2} \sum_{\mathbf{q}\nu} \epsilon_{\mathbf{q}\nu}^\dagger M \epsilon_{\mathbf{q}\nu}. \tag{9}$$

In equilibrium, we know $\langle a_{\mathbf{q}\nu}^\dagger a_{\mathbf{q}\nu'} \rangle = n_{\mathbf{q}\nu}\delta_{\nu\nu'}$ [n the phonon occupation, Bose-Einstein (BE) at thermal equilibrium], and so we can express the total angular momentum as

$$\mathcal{J}_z = \sum_{\mathbf{q}\nu} \epsilon_{\mathbf{q}\nu}^\dagger M \epsilon_{\mathbf{q}\nu} \hbar(n_{\mathbf{q}\nu} + 1/2) \equiv \sum_{\mathbf{q}\nu} \ell_{\mathbf{q}\nu}^s (n_{\mathbf{q}\nu} + 1/2), \tag{10}$$

where the phonon angular momenta at $\mathbf{q}$ are given by $\ell_{\mathbf{q}\nu}^s$. We emphasize that there are two contributions to the total phonon angular momentum ℓ^{ph}: (i) the local part yielding spin PAM ℓ^s, coming from the eigendisplacements ϵ and (ii) the nonlocal part determined by $e^{i\mathbf{R}_\ell \cdot \mathbf{q}}$ yielding orbital PAM ℓ^0. The sum of

these contributions for each oscillating sublattice yields the total phonon PAM.

Note that this implies at $T = 0$, each mode and momenta, the phononic system has a zero-point spin PAM of $(\hbar/2)\epsilon_{\mathbf{q}\nu}^{\dagger} M \epsilon_{\mathbf{q}\nu}$, in addition to the zero-point energy $\hbar\omega_{\mathbf{q}\nu}/2$. Taylor expanding the BE distribution $\{e^x - 1\}^{-1} \simeq 1/x - 1/2 + x/12 + \cdots$, we find

$$\mathcal{J}_z(T \to \infty) = \sum_{\mathbf{q}\nu} \left\{ \frac{k_B T}{\hbar\omega_{\mathbf{q}\nu}} + \frac{\hbar\omega_{\mathbf{q}\nu}}{12 k_B T} \right\} \ell_{\mathbf{q}\nu}^s. \quad (11)$$

Noting the completeness relation $\sum_{\nu} \epsilon_{\mathbf{q}\nu}^{\dagger} \otimes \epsilon_{\mathbf{q}\nu} = \mathbb{1}_{2n \times 2n}$, the closure relation for these orthonormal atomic displacements can be shown [49] to yield

$$\sum_{\nu} \frac{(\epsilon_{\mathbf{q}\nu})^i (\epsilon_{\mathbf{q}\nu}^*)^j}{\omega_{\mathbf{q}\nu}} = 0. \quad (12)$$

We finally show that at high temperature, there cannot be spin angular momentum in the system. This is consistent with the notion that at high temperature, atoms are equally likely to be displaced in all directions, yielding canceling contributions to the spin PAM.

$$\lim_{T \to \infty} \mathcal{J}_z(T) = \sum_{\mathbf{q}\nu} \ell_{\mathbf{q}\nu}^s \frac{k_B T}{\hbar\omega_{\mathbf{q}\nu}} + \ell_{\mathbf{q}\nu}^s \frac{\hbar\omega_{\mathbf{q}\nu}}{k_B T}$$

$$= \sum_{\substack{\mathbf{q} \\ j,i}} M_{ji} \underbrace{\sum_{\nu} \frac{(\epsilon_{\mathbf{q}\nu})^i (\epsilon_{\mathbf{q}\nu}^*)^j}{\omega_{\mathbf{q}\nu}}}_{} \nearrow^{0} T + \frac{1}{k_B T} \ell_{\mathbf{q}\nu}^s \hbar\omega_{\mathbf{q}\nu} = 0$$

$$(13)$$

where the arrow indicates that the term identically evaluates to zero. There are additional constraints on this PAM that restrict the presence of chiral phonons in standard systems. Firstly, conservation of angular momentum dictates that the spin angular momentum of the phonon modes must cancel, namely,

$$\sum_{\nu} \ell_{\mathbf{q}\nu}^s = \sum_{\nu} \epsilon_{\mathbf{q}\nu}^{\dagger} M \epsilon_{\mathbf{q}\nu} \hbar$$

$$= i\hbar \sum_{\nu} \sum_{\alpha} [(\epsilon_{\mathbf{q}\nu,\alpha}^*)^y (\epsilon_{\mathbf{q}\nu,\alpha})^x - (\epsilon_{\mathbf{q}\nu,\alpha}^*)^x (\epsilon_{\mathbf{q}\nu,\alpha})^y]$$

$$= 0. \quad (14)$$

Furthermore, there cannot be phonon PAM in systems with no spin-phonon interaction. In such systems, we completely describe the trivial phonon system by solving the dynamical matrix equation $\hat{D}(\mathbf{q})\epsilon_{\mathbf{q}\nu} = \omega_{\mathbf{q}\nu}^2 \epsilon_{\mathbf{q}\nu}$. In such a system, the eigenvalues and eigenvectors satisfy $\omega_{-\mathbf{q}\nu} = \omega_{\mathbf{q}\nu}$ and $\epsilon_{-\mathbf{q}\nu} = \epsilon_{\mathbf{q}\nu}$ respectively. Noting $M^T = -M$, one can show $\ell_{-\mathbf{q}\nu}^s = -\ell_{\mathbf{q}\nu}^s$, and using the fact the $n_{-\mathbf{q}\nu} = n_{\mathbf{q}\nu}$ we find $\mathcal{J}_z \equiv 0$. In systems with spin-phonon interaction, the dynamical matrix equation will be of the form $[(-i\omega + A)^2 + D]\epsilon = 0$, and time-reversal symmetry will be explicitly broken, allowing $\mathcal{J}_z \neq 0$.

In practice, stating that phonons can have PAM does not inherently bridge these theoretical predictions with an experimentally accessible phenomenon. To determine how these chiral phonons manifest themselves in the lattice, we perform

a basis transformation on the atomic displacements ϵ as follows. Let the new basis be

$$|R_1\rangle \equiv \frac{1}{\sqrt{2}}(1 \; i \; 0 \; \cdots \; 0)^T, \quad |L_1\rangle \equiv \frac{1}{\sqrt{2}}(1 \; -i \; 0 \; \cdots \; 0)^T,$$

$$|R_n\rangle \equiv \frac{1}{\sqrt{2}}(0 \; \cdots \; 0 \; 1 \; i)^T \quad, |L_n\rangle \equiv \frac{1}{\sqrt{2}}(0 \; \cdots \; 0 \; 1 \; -i)^T.$$

$$(15)$$

We can define the coefficients of the basis transformation $\epsilon_{R_\alpha} = \langle R_\alpha | \epsilon \rangle = (x_\alpha - iy_\alpha)/\sqrt{2}$ and $\epsilon_{L_\alpha} = \langle L_\alpha | \epsilon \rangle = (x_\alpha + iy_\alpha)/\sqrt{2}$ such that [50] $\epsilon = \sum_\alpha \epsilon_{R_\alpha} |R_\alpha\rangle + \epsilon_{L_\alpha} |L_\alpha\rangle$. We note that we can define the phonon circular polarization operator

$$\hat{S}_z^{\text{ph}} \equiv \sum_\alpha (|R_\alpha\rangle\langle R_\alpha| - |L_\alpha\rangle\langle L_\alpha|) = \begin{pmatrix} 0 & -i \\ i & 0 \end{pmatrix} \otimes \mathbb{1}_{n \times n}, \quad (16)$$

which is identically equal to the M matrix from before. We can therefore compute the phonon polarization s_z^{ph} as

$$s_z^{\text{ph}} = \sum_\alpha (|\epsilon_{R_\alpha}|^2 - |\epsilon_{L_\alpha}|^2)\hbar = \epsilon^{\dagger} \hat{S}_z \epsilon \hbar = \epsilon^{\dagger} M \epsilon \hbar \equiv \ell_z^s. \quad (17)$$

This shows that phonon circular polarization and phonon spin angular momenta are entirely equivalent in this formalism. Namely, phonons with nonzero PAM must inherently induce circular atomic orbits, see Figs. 2(a) and 2(b). By characterizing those modes with nonzero PAM, we can then exactly determine the corresponding real space motion of the atoms in the 2D material.

IV. GENERATION OF CHIRAL PHONONS

By using ultrashort pulses of circularly polarized light, spin-conserving interband electronic transitions can be driven that impulsively photodope carriers into either the K (σ^+) or K' (σ^-) valley of monolayer TMDs. This nonequilibrium distribution of valley-polarized carriers will depolarize as the carrier distribution thermalizes to the band edges through allowed momentum and energy relaxation channels.

Equation 5 shows that linearly polarized photoexcitation (polarization state $(|L\rangle + |R\rangle)/\sqrt{2}$) induces interband electronic transitions at the band edges with equal amplitude at time-reversal related K and K' valleys. The subsequent relaxation of the (hot) charge carriers back to the band edges occurs through interactions with phonons and is determined by the magnitude of the EPC matrix elements $|g_{mn\nu}(\mathbf{k}, \mathbf{q})|^2$, where m, n (ν) index electronic bands (phonon dispersion modes) at electronic (phononic) momentum $\mathbf{k}$ ($\mathbf{q}$). This coupling may be screened by ambient conditions, such as the dielectric environment to which 2D materials are more susceptible, leading to a renormalization of the EPC strength [27].

Only the ultrafast lattice and charge carrier dynamics following linearly polarized above band-gap photoexcitation have been previously studied, either with *ab initio* methods [47] or ultrafast electron diffuse scattering techniques in 1L-MoS$_2$ [27]. Here, the ultrafast relaxation results in a phonon population distribution that is profoundly anisotropic in momentum but has no momentum-valley polarization. Circularly polarized light and the associated (initial) valley polarized carrier distribtuion change the resulting dynamics
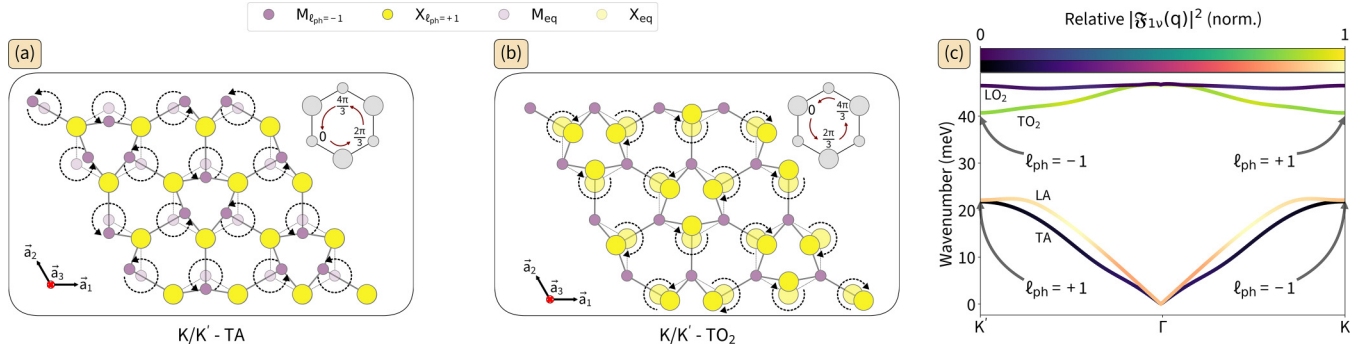
FIG. 2. Chiral phonon in 1L-MX$_2$ materials. (a) The TA chiral phonon at the K point ($\ell_{ph} = -1$). The transition metal precesses in a circular orbit about its average position in thermal equilibrium, while the chalcogen atoms are static. (b) The TO$_2$ chiral phonon at the K point ($\ell_{ph} = +1$). The chalcogens orbit clockwise and the transition metal remains static. Inset on the top right of each panel is the relative phase of the atomic movements. (c) Phonon normal mode dispersion of chiral (acoustic and E' optical) phonon branches in 1L-MX_2 materials. The relative strength of the one-phonon structure factor for these modes is given by the coloration for the acoustic and optical branches respectively. Note that these modes are the brightest in the proposed UEDS experiment, and are responsible for (non)chiral charge carrier scattering (T-polarized for chiral scattering, L-polarized for nonchiral scattering). The Z-polarized modes are not visible in the geometry proposed and the single phonon structure factor of the E'' optical modes are much smaller than for the E' modes shown. The chirality at K of the TA and TO$_2$ modes are labeled, with the chiralities flipping sign at K' owing to the time-reversal symmetry.

profoundly compared to linear polarized excitation. Intervalley momentum and energy relaxation of electrons in the conduction band at K (or K') can only occur via scattering with a chiral phonon of momentum K' (or K) that connects the K valleys [Fig. 1(b)]. Intervalley momentum and energy relaxation of holes in the valence band at K (or K') can only occur via scattering with nonchiral phonons of momentum K (or K') that connects the K (or K') and Γ valleys [Fig. 1(b)]. Thus, on the picosecond timescale associated with rapid EPC processes, a profoundly momentum-valley polarized phonon distribution is expected. Namely, chiral phonons are expected in the K valley opposite to the initially prepared valley, while nonchiral phonons are expected in the K valley into which carriers were pumped. It is worth noting that in W-based monolayer TMDs, the hole relaxation channel is not present due to the large $\Gamma - K$ valley energy splitting in the valence band, resulting in a "pure" momentum-valley polarized chiral phonon distribution.

In the next section, we describe how ultrafast phonon diffuse scattering techniques can be used to read out the nonequilibrium momentum-valley polarized phonon distribution that follows circularly polarized excitation in monolayer TMDs.

V. OBSERVATION OF PHONON MOMENTUM POLARIZATION VIA ULTRAFAST PHONON DIFFUSE SCATTERING

Ultrafast phonon diffuse scattering can be used to determine the nonequilibrium populations of phonon modes across the entire BZ in a single crystal material with femtosecond time resolution [19,51]. This information can be used to determine the strength of the wave-vector-dependent (or momentum-dependent) coupling between electrons and phonons and the strength of anharmonic coupling and other three-phonon processes that lead to thermalization within the phonon system. While either x-ray or electron phonon diffuse

scattering can be used, we focus herein on ultrafast electron diffuse scattering (UEDS) since the $\sim 10^5$ enhancement in atomic scattering cross section [52] is of great benefit to the observation of weak phonon diffuse signals from monolayer samples.

In such experiments, phonons are initially thermally populated according to the BE distribution at the base experimental temperature before photoexcitation. Phonon excitations create a nontrivial density-density correlation that is probed by the scattering bunch, recorded in transmission on a detector as a function of the momentum transfer (scattering vector) between the scatterers and the lattice $\mathbf{Q} \equiv \mathbf{k}_i - \mathbf{k}_f$. The intensity of this scattering pattern (i.e., number of electrons scattered to each pixel of the detector) as a function of momentum transfer, $I_{\mathrm{all}}(\mathbf{Q})$, can be approximated as a series expansion as follows [16]:

$$I_{\mathrm{all}}(\mathbf{Q}) = I_0(\mathbf{Q}) + I_1(\mathbf{Q}) + \cdots, \tag{18}$$

where $I_0(\mathbf{Q})$ is the elastic "Bragg" scattering, and $I_1(\mathbf{Q})$ is the inelastic single "phonon diffuse" scattering. Adopting phonon normal mode coordinates gives

$$I_1(\mathbf{Q}) \propto \sum_{\nu} \frac{n_{\mathbf{q}\nu} + 1/2}{\omega_{\mathbf{q}\nu}} |\mathfrak{F}_{1\nu}(\mathbf{Q})|^2, \tag{19}$$

where the label ν indicates the specific phonon mode, $\mathbf{Q}$ is the electron scattering vector, $\mathbf{q}$ is the reduced phonon wave vector (i.e., $\mathbf{q} = \mathbf{Q} - \mathbf{H}$, where $\mathbf{H}$ is the closest Bragg peak), and $n_{\mathbf{q}\nu}$ is the mode-resolved occupancy with energy $\hbar\omega_{\mathbf{q}\nu}$. As this single phonon diffuse scattering term depends solely on phonons at wave vector $\mathbf{q}$, it is a direct measure of the phonon occupancy distribution at that wave vector. This single-phonon scattering framework is a good approximation for UEDS on monolayer TMDs near room temperature, but a full multiphonon scattering formalism has also recently been developed to interpret UEDS data [53].

TABLE II. Chirality of phonons in 1L-MoS$_2$. The symmetries of each oscillation are given by the label and C_{3h} point group representation where applicable. Circular polarizations and spin pseudo-angular momentum of Mo (S) are given by s^z_{Mo} (s^z_S) and ℓ^s_{Mo} (ℓ^s_S), respectively. Phonon angular momentum is given by ℓ_{ph} and the parity of the mirror symmetry of each mode is given by M_s.

ν	Label	D_{3h}	ω_K[a]	s^z_{Mo}	s^z_S	ℓ^s_{Mo}[b]	ℓ^s_S[b]	ℓ_{ph}[b]	M_s[c]
1	ZA	A_2	21.791	0	−0.325	0	−1	1	−1
2	TA		22.096	0.552	0	1	0	−1	1
3	LA		28.219	−0.301	0.348	−1	1	0	1
4	TO$_1$	E''	40.959	0	0	0	0	0	−1
5	LO$_1$	E''	40.064	0	0.500	0	1	0	1
6	TO$_2$	E'	40.664	0	−0.500	0	−1	1	1
7	LO$_2$	E'	46.458	−0.206	0.397	−1	1	0	1
8	ZO$_2$	A_1	48.886	0.083	0	1	0	−1	1
9	ZO$_1$	A''_2	45.803	0	−0.412	0	−1	1	−1

[a]In units of meV.
[b]In units of $\hbar$.
[c]Mirror symmetry is with respect to the x-y plane.

The $\mathfrak{F}_{1\nu}$ are known as the "single-phonon structure factors," geometric weights that describe the relative strength of scattering from different phonon modes:

$$|\mathfrak{F}_{1\nu}(\mathbf{Q})|^2 = \left| \sum_{\kappa} e^{-W_\kappa(\mathbf{Q})} \frac{f_\kappa(\mathbf{Q})}{\sqrt{\mu_\kappa}} (\mathbf{Q} \cdot \mathbf{e}_{\mathbf{q}\nu\kappa}) \right|^2, \quad (20)$$

where κ is the atomic index, W_κ is the well-known Debye-Waller factor [54,55], f_κ the atomic scattering cross-section for electrons, and μ the effective atomic mass. The critical term here is the dot product $(\mathbf{Q} \cdot \mathbf{e}_{q\kappa})$, which shows that the contribution of a particular phonon mode is enhanced (suppressed) when the corresponding atomic polarization(s) are parallel (perpendicular) to the scattering vector, showing a sensitive dependence on the atomic polarization vectors $\{\mathbf{e}_{\mathbf{q}\nu\kappa}\}$ [19]. Further, $\mathfrak{F}_{1\nu}(\mathbf{Q})$ are relatively large when the phonon mode ν is polarized parallel to the reduced scattering vector $\mathbf{q}$. This implies that, despite the fact that these experiments are inherently energy-integrated, by inspection of the diffuse pattern at particular $\mathbf{Q}$, one is able to extract mode-resolved information from the diffuse pattern at finite phonon momentum $\mathbf{q}$.

As a prototypical spin- and valleytronic 2D hexagonal material, here we examine UEDS as a probe of chiral phonons in 1L-MoS$_2$. Standard density functional perturbation theory (DFPT) allows for computation of the atomic polarization vectors for each phonon mode, computed using the code suites of QUANTUM ESPRESSO [56,57]. We can compute the phonon PAM of each mode by the sum of orbital and spin components for each sublattice that is oscillating for the valley phonons. Doing so, we obtain the chart in Table II.

The modes with nonzero PAM must jointly satisfy $\{\nu | \ell_{ph} \neq 0 \cup M_s \equiv 1\}$, where even parity of the in-plane mirror symmetry is needed to not get canceling contributions to the PAM from different locations in the supercell. This allows for the identification of three chiral modes in this system. For chirality $+1$ (in units of $\hbar$), there is only the transverse optical mode of E' symmetry (TO$_2$), corresponding to the sulfur sublattice oscillating clockwise. For chirality -1, we identify both the transverse acoustic (TA) mode and Z-polarized opti-

cal mode of A_1 symmetry (ZO$_2$). Both these modes involve the oscillation of the moldybdenum sublattice in an anticlockwise direction, but the ZO$_2$ mode has a much lower degree of polarization (by an order of magnitude) and will not be as readily excited in the generation schemes proposed here.

For the case of monolayer TMDs, the phonon scattering selection rules mean that $\mathfrak{F}_{1\nu}$ for the out-of-plane (Z-polarized) modes and the optical modes of E'' symmetry are very weak in the geometry of these experiments (along the [001] direction). These experiments primarily probe the $\mathbf{q}$-dependent population dynamics of the E' optical and LA/TA modes, which are exactly the modes that are characterized by $\ell_{ph} \neq 0$. The only assumption made in Eqs. (19) and (20) is that single phonon scattering dominates the diffuse intensity. In this single-phonon scattering approximation, we compute the scattering intensities for phonons of chirality ± 1 within the Laval-Born-James theory [58–60] using modified versions of the codes in the EPW/ZG suite of QUANTUM ESPRESSO. Band-structure calculations used fully relativistic norm-conserving Troullier-Martins pseudopotentials [61] and the Perdew-Burke-Ernzerhof generalized-gradient approximation for the exchange-correlation functional [62]. We employed a planewave energy cutoff of 120 Ry, and a $20 \times 20 \times 1$ Monkhorst-Pack $\mathbf{k}$ grid for the monolayer, and $20 \times 20 \times 20$ for the bulk. In order to avoid spurious interactions among periodic replicas of the monolayers in the out-of-plane direction, an interlayer vacuum spacing of 18 Å and truncated coulomb interaction were employed [63]. For all calculations, we used the primitive cell of MoS$_2$, with relaxed lattice parameter of 3.16 Å. Second-order interatomic force constants were computed using DFPT on an $8 \times 8 \times 1$ $\mathbf{q}$ grid for 1L-MoS$_2$, and a $4 \times 4 \times 4$ $\mathbf{q}$ grid for bulk MoS$_2$ and Fourier interpolated onto a $256 \times 256 \times 1$ $\mathbf{q}$ grid to compute phonon normal mode dispersions and thus the diffuse scattering patterns.

In this work, we make no attempt to perform a full simulation of the nonequilibrium chiral carrier-phonon interactions that following circularly polarized excitation in 1L-MoS$_2$. Instead, we present a simplified, but qualitatively accurate model for the nonequilibrium phonon populations that
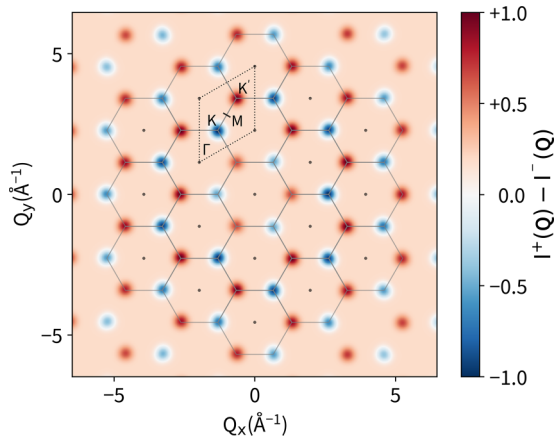
FIG. 3. The diffuse scattering intensity dichroism induced by charge carrier depolarization following circularly polarized photoexcitation, taken as $I^+ - I^-$. A selection of BZs are outlined, with the dots representing the Γ points, emphasizing the locality of the features around the K valleys.

FIG. 4. Relative percent difference of bulk diffuse scattering versus monolayer scattering $(I_{bulk}^1 - I_{ml}^1)/I_{bulk}^1$. There is clear structure across the image showing significant changes in diffuse scattering between multilayer and monolayer, but there are no features around the K valleys, indicating that the observation of chiral phonons cannot be done in an equilibrium measurement.

result transiently from valley depolarization driven by inelastic chiral carrier-phonon scattering in order to determine the observable impact on UEDS patterns. To model the effect of the momentum-valley polarized phonon occupations following carrier valley depolarization, we take the nonchiral modes to be occupied according to the BE distribution at room temperature and the chiral modes involved in valley depolarization at an elevated "effective temperature" of 380 K within a Gaussian window of full width half max (FWHM) 0.1 reduced lattice units [64] around K (K'). The qualitative features in the diffuse scattering pattern are not sensitive to the precise values of these temperatures. Using the framework described above, we compute UEDS patterns under the nonthermal occupation of phonons.

The signature of chiral phonon emission is the relative diffuse intensities at the K (K') valleys. We can define the phonon momentum-valley anisotropy as

$$\eta(\tau) = \frac{I_1(\mathbf{q} = K', \tau) - I_1(\mathbf{q} = K, \tau)}{I_1(\mathbf{q} = K', \tau) + I_1(\mathbf{q} = K, \tau)}. \tag{21}$$

For initial carrier polarization at K, pump-probe delay times where $\eta > 0$ are indicative of dynamics dominated by a K' chiral phonon assisted conduction electron K-K' scattering, as opposed to $\eta < 0$ where nonchiral assisted valence hole K-Γ scattering is dominant.

The differential diffuse scattering intensity predicted for photoexcitation of handedness σ^+ (thus $\ell_{ph} = -1$, the TA mode with occupancy centered at K') minus σ^- (thus $\ell_{ph} = +1$, the TO$_2$ mode with occupancy centered at K) is shown in Fig. 3, where we define $\mathcal{I}^+$ ($\mathcal{I}^-$) as the scattering intensity resulting from σ^+ (σ^-) handed photoexcitation. The differential pattern shows clear features at the K points associated with nonequilibrium populations of chiral phonons that should be measurable in circularly polarized pump-probe experiments. The time constants associated with the red (K') and blue (K) intensity features in Fig. 3 provides a measure of the strength of chiral carrier-phonon coupling to the TA and TO$_2$ chiral modes respectively. Further, the
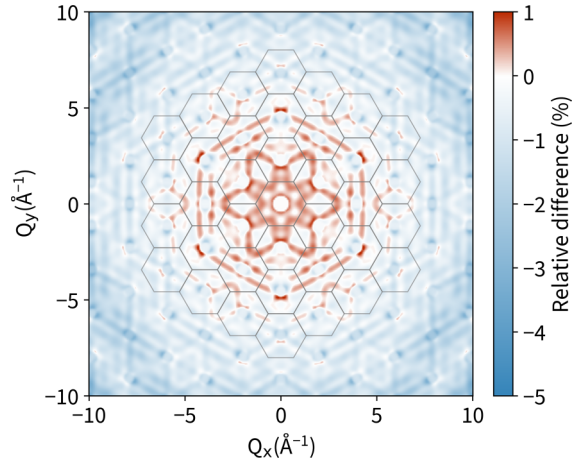
intensity contrast visible in Fig. 3 is reduced (or disappears entirely) if carrier valley-depolarization occurs by means unrelated to inelastic phonon scattering on a timescale shorter than that associated with EPC, e.g., via the exchange interaction. Thus these observable features in the differential phonon diffuse intensity provide a sensitive test of phonon-assisted valley depolarization in monolayer TMDs, allowing for the identification of regimes in time and values of n_0 where chiral phonon emission, electron-hole exchange, or carrier-carrier scattering become dominant with regards to the charge carrier depolarization.

The profound impact of the nonequilibrium momentum-valley polarized chiral phonon populations on diffuse scattering contrast in K and K' regions that emerges transiently during valley depolarization of the carrier system due to EPC (Fig. 3) can be contrasted with the expected differences in phonon diffuse scattering between monolayer and bulk samples at thermal equilibrium. Chiral phonons manifest in monolayer TMDs, with distinct phonon diffuse signatures in momentum space, even at thermal equilibrium. However, the momentum anisotropy due to chiral phonons is not evident in the differential diffuse scattering intensity comparing bulk and monolayer MoS$_2$ at thermal equilibrium shown in Fig. 4. There are intensity contrasts visible in this difference pattern, but none at momentum positions associated with the K-point chiral modes, thus necessitating nonequilibrium measurements to observe chiral phonon emission.

VI. CONCLUSIONS

The properties of monolayer hexagonal lattices have been shown to yield chiral electron-phonon interactions that can be a key feature of carrier valley depolarization processes following photoexcitation with circularly polarized light. The allowed momentum and energy relaxation processes involved populate valley-polarized, nonequilibrium distributions of

chiral phonons whose circular atomic oribts and angular momentum are required to conserve total angular momentum of the coupled electron-lattice system during valley depolarization. Further, these chiral carrier-phonons interactions are uniquely hallmarked by increases in chiral phonon occupancy at either K or K' points in the BZ. As a state-of-the-art technique for the direct measurement of nonequilibrium phonon occupancy with full momentum resolution, UEDS can directly identify the resulting valley polarized chiral phonon distributions in a pump-probe experiment. Further, the technique will also be able to distinguish between chiral and nonchiral dominated scattering regimes occurring on the picosecond timescale provided data of sufficient signal-to-noise ratio and sample quality.

[1] B. T. Zhou, K. Taguchi, Y. Kawaguchi, Y. Tanaka, and K. T. Law, Spin-orbit coupling induced valley hall effects in transition-metal dichalcogenides, Commun. Phys. **2**, 26 (2019).

[2] A. Molina-Sánchez, D. Sangalli, K. Hummer, A. Marini, and L. Wirtz, Effect of spin-orbit interaction on the optical spectra of single-layer, double-layer, and bulk MoS_2, Phys. Rev. B **88**, 045412 (2013).

[3] D. Xiao, G.-B. Liu, W. Feng, X. Xu, and W. Yao, Coupled Spin and Valley Physics in Monolayers of MoS_2 and Other Group-vi Dichalcogenides, Phys. Rev. Lett. **108**, 196802 (2012).

[4] H. Beyer, G. Rohde, A. Grubišić Čabo, A. Stange, T. Jacobsen, L. Bignardi, D. Lizzit, P. Lacovig, C. E. Sanders, S. Lizzit, K. Rossnagel, P. Hofmann, and M. Bauer, 80% Valley Polarization of Free Carriers in Singly Oriented Single-Layer WS_2 on au(111), Phys. Rev. Lett. **123**, 236802 (2019).

[5] D. Y. Qiu, F. H. da Jornada, and S. G. Louie, Optical Spectrum of MoS_2: Many-Body Effects and Diversity of Exciton States, Phys. Rev. Lett. **111**, 216805 (2013).

[6] W. Yao, D. Xiao, and Q. Niu, Valley-dependent optoelectronics from inversion symmetry breaking, Phys. Rev. B **77**, 235406 (2008).

[7] Z. Y. Zhu, Y. C. Cheng, and U. Schwingenschlögl, Giant spin-orbit-induced spin splitting in two-dimensional transition-metal dichalcogenide semiconductors, Phys. Rev. B **84**, 153402 (2011).

[8] K. Kośmider, J. W. González, and J. Fernández-Rossier, Large spin splitting in the conduction band of transition metal dichalcogenide monolayers, Phys. Rev. B **88**, 245436 (2013).

[9] A. Kormányos, V. Zólyomi, N. D. Drummond, and G. Burkard, Spin-Orbit Coupling, Quantum Dots, and Qubits in Monolayer Transition Metal Dichalcogenides, Phys. Rev. X **4**, 011034 (2014).

[10] E. S. Kadantsev and P. Hawrylak, Electronic structure of a single MoS_2 monolayer, Solid State Commun. **152**, 909 (2012).

[11] Y. Song and H. Dery, Transport Theory of Monolayer Transition-Metal Dichalcogenides through Symmetry, Phys. Rev. Lett. **111**, 026601 (2013).

[12] E. Lefrançois, G. Grissonnanche, J. Baglo, P. Lampen-Kelley, J.-Q. Yan, C. Balz, D. Mandrus, S. E. Nagler, S. Kim, Y.-J. Kim, N. Doiron-Leyraud, and L. Taillefer, Evidence of a Phonon Hall effect in the Kitaev Spin Liquid Candidate $\alpha-rucl_3$, Phys. Rev. X **12**, 021025 (2022).

[13] G. Grissonnanche, A. Legros, S. Badoux, E. Lefrançois, V. Zatko, M. Lizaire, F. Laliberté, A. Gourgout, J.-S. Zhou, S. Pyon, T. Takayama, H. Takagi, S. Ono, N. Doiron-Leyraud, and L. Taillefer, Giant thermal hall conductivity in the pseudogap phase of cuprate superconductors, Nature (London) **571**, 376 (2019).

[14] T. Uehara, T. Ohtsuki, M. Udagawa, S. Nakatsuji, and Y. Machida, Phonon thermal hall effect in a metallic spin ice, Nat. Commun. **13**, 4604 (2022).

[15] Y. Hirokane, Y. Nii, Y. Tomioka, and Y. Onose, Phononic thermal hall effect in diluted terbium oxides, Phys. Rev. B **99**, 134419 (2019).

[16] D. Filippetto, P. Musumeci, R. K. Li, B. J. Siwick, M. R. Otto, M. Centurion, and J. P. F. Nunes, Ultrafast electron diffraction: Visualizing dynamic states of matter, Rev. Mod. Phys. **94**, 045004 (2022).

[17] M. J. Stern, L. P. René de Cotret, M. R. Otto, R. P. Chatelain, J.-P. Boisvert, M. Sutton, and B. J. Siwick, Mapping momentum-dependent electron-phonon coupling and nonequilibrium phonon dynamics with ultrafast electron diffuse scattering, Phys. Rev. B **97**, 165416 (2018).

[18] M. Trigo, M. Fuchs, J. Chen, M. Jiang, M. Cammarata, S. Fahy, D. M. Fritz, K. Gaffney, S. Ghimire, A. Higginbotham *et al.*, Fourier-transform inelastic x-ray scattering from time-and momentum-dependent phonon–phonon correlations, Nat. Phys. **9**, 790 (2013).

[19] L. P. René de Cotret, J.-H. Pöhls, M. J. Stern, M. R. Otto, M. Sutton, and B. J. Siwick, Time- and momentum-resolved phonon population dynamics with ultrafast electron diffuse scattering, Phys. Rev. B **100**, 214115 (2019).

[20] L. Waldecker, R. Bertoni, H. Hübener, T. Brumme, T. Vasileiadis, D. Zahn, A. Rubio, and R. Ernstorfer, Momentum-Resolved View of Electron-Phonon Coupling in Multilayer WSe_2, Phys. Rev. Lett. **119**, 036803 (2017).

[21] T. Chase, M. Trigo, A. H. Reid, R. Li, T. Vecchione, X. Shen, S. Weathersby, R. Coffee, N. Hartmann, D. A. Reis, X. J. Wang, and H. A. Dürr, Ultrafast electron diffraction from nonequilibrium phonons in femtosecond laser heated Au films, Appl. Phys. Lett. **108**, 041909 (2016).

[22] H. Seiler, D. Zahn, M. Zacharias, P.-N. Hildebrandt, T. Vasileiadis, Y. W. Windsor, Y. Qi, C. Carbogno, C. Draxl, R. Ernstorfer, and F. Caruso, Accessing the anisotropic nonthermal

phonon populations in black phosphorus, Nano Lett. **21**, 6171 (2021).

[23] M. R. Otto, J.-H. Pöhls, L. P. René de Cotret, M. J. Stern, M. Sutton, and B. J. Siwick, Mechanisms of electron-phonon coupling unraveled in momentum and time: The case of soft phonons in TiSe$_2$, Sci. Adv. **7**, eabf2810 (2021).

[24] L. P. René de Cotret, M. R. Otto, J.-H. Pöhls, Z. Luo, M. G. Kanatzidis, and B. J. Siwick, Direct visualization of polaron formation in the thermoelectric snse, Proc. Natl. Acad. Sci. **119**, e2113967119 (2022).

[25] H. Chen, W. Wu, J. Zhu, S. A. Yang, and L. Zhang, Propagating chiral phonons in three-dimensional materials, Nano Lett. **21**, 3060 (2021).

[26] H. Zhu, J. Yi, M.-Y. Li, J. Xiao, L. Zhang, C.-W. Yang, R. A. Kaindl, L.-J. Li, Y. Wang, and X. Zhang, Observation of chiral phonons, Science **359**, 579 (2018).

[27] T. L. Britt, Q. Li, L. P. René de Cotret, N. Olsen, M. Otto, S. A. Hassan, M. Zacharias, F. Caruso, X. Zhu, and B. J. Siwick, Direct view of phonon dynamics in atomically thin MoS$_2$, Nano Lett. **22**, 4718 (2022).

[28] J. Wilson and A. Yoffe, The transition metal dichalcogenides discussion and interpretation of the observed optical, electrical and structural properties, Adv. Phys. **18**, 193 (1969).

[29] M.-C. Chang and Q. Niu, Berry phase, hyperorbits, and the hofstadter spectrum: Semiclassical dynamics in magnetic bloch bands, Phys. Rev. B **53**, 7010 (1996).

[30] A. Kormányos, V. Zólyomi, N. D. Drummond, P. Rakyta, G. Burkard, and V. I. Fal'ko, Monolayer MoS$_2$: Trigonal warping, the Γ valley, and spin-orbit coupling effects, Phys. Rev. B **88**, 045416 (2013).

[31] A. Kormányos, G. Burkard, M. Gmitra, J. Fabian, V. Zólyomi, N. D. Drummond, and V. Fal'ko, $\mathbf{k} \cdot \mathbf{p}$ theory for two-dimensional transition metal dichalcogenide semiconductors, 2D Mater. **2**, 022001 (2015).

[32] R. Winkler, *Spin-orbit Coupling Effects in Two-Dimensional Electron and Hole Systems* (Springer, Berlin, 2003).

[33] D. Xiao, M.-C. Chang, and Q. Niu, Berry phase effects on electronic properties, Rev. Mod. Phys. **82**, 1959 (2010).

[34] Note, spins are completely decoupled and so the spin quantum number s_z (eigenvalues $s_z = \pm 1$ of the spin Pauli matrix $\hat{s}_z$) remains a good quantum number.

[35] H. Zeng, J. Dai, W. Yao, D. Xiao, and X. Cui, Valley polarization in MoS$_2$ monolayers by optical pumping, Nat. Nanotechnol. **7**, 490 (2012).

[36] A. M. Jones, H. Yu, N. J. Ghimire, S. Wu, G. Aivazian, J. S. Ross, B. Zhao, J. Yan, D. G. Mandrus, D. Xiao, W. Yao, and X. Xu, Optical generation of excitonic valley coherence in monolayer WSe$_2$, Nat. Nanotechnol. **8**, 634 (2013).

[37] X. Xu, W. Yao, D. Xiao, and T. F. Heinz, Spin and pseudospins in layered transition metal dichalcogenides, Nat. Phys. **10**, 343 (2014).

[38] S. Ulstrup, A. G. Cabo, D. Biswas, J. M. Riley, M. Dendzik, C. E. Sanders, M. Bianchi, C. Cacho, D. Matselyukh, R. T. Chapman, E. Springate, P. D. C. King, J. A. Miwa, and P. Hofmann, Spin and valley control of free carriers in single-layer WS$_2$, Phys. Rev. B **95**, 041405(R) (2017).

[39] L. T. Lloyd, R. E. Wood, F. Mujid, S. Sohoni, K. L. Ji, P.-C. Ting, J. S. Higgins, J. Park, and G. S. Engel, Sub-10 fs intervalley exciton coupling in monolayer MoS$_2$ revealed

by helicity-resolved two-dimensional electronic spectroscopy, ACS Nano **15**, 10253 (2021).

[40] A. Steinhoff, M. Florian, M. Rösner, M. Lorke, T. O. Wehling, C. Gies, and F. Jahnke, Nonequilibrium carrier dynamics in transition metal dichalcogenide semiconductors, 2D Mater. **3**, 031006 (2016).

[41] M. Selig, F. Katsch, R. Schmidt, S. Michaelis de Vasconcellos, R. Bratschitsch, E. Malic, and A. Knorr, Ultrafast dynamics in monolayer transition metal dichalcogenides: Interplay of dark excitons, phonons, and intervalley exchange, Phys. Rev. Res. **1**, 022007(R) (2019).

[42] R. L. Wilmington, H. Ardekani, A. Rustagi, A. Bataller, A. F. Kemper, R. A. Younts, and K. Gundogdu, Fermi liquid theory sheds light on hot electron-hole liquid in $1l - Mos_2$, Phys. Rev. B **103**, 075416 (2021).

[43] A. Chernikov, C. Ruppert, H. M. Hill, A. F. Rigosi, and T. F. Heinz, Population inversion and giant bandgap renormalization in atomically thin Ws$_2$ layers, Nat. Photonics **9**, 466 (2015).

[44] A. Steinhoff, M. Florian, M. Rösner, G. Schönhoff, T. O. Wehling, and F. Jahnke, Exciton fission in monolayer transition metal dichalcogenide semiconductors, Nat. Commun. **8**, 1166 (2017).

[45] G. L. Bir, A. G. Aronov, and G. E. Pikus, Spin relaxation of electrons due to scattering by holes, Sov. Phys. JETP **42**, 705 (1975).

[46] A. I. Prazdnichnykh, M. M. Glazov, L. Ren, C. Robert, B. Urbaszek, and X. Marie, Control of the exciton valley dynamics in atomically thin semiconductors by tailoring the environment, Phys. Rev. B **103**, 085302 (2021).

[47] F. Caruso, Nonequilibrium lattice dynamics in monolayer MoS$_2$, J. Phys. Chem. Lett. **12**, 1734 (2021).

[48] R. Bertoni, C. W. Nicholson, L. Waldecker, H. Hübener, C. Monney, U. De Giovannini, M. Puppin, M. Hoesch, E. Springate, R. T. Chapman, C. Cacho, M. Wolf, A. Rubio, and R. Ernstorfer, Generation and Evolution of Spin-, Valley-, and Layer-Polarized Excited Carriers in Inversion-Symmetric WSe$_2$, Phys. Rev. Lett. **117**, 277201 (2016).

[49] L. Zhang and Q. Niu, Angular Momentum of Phonons and the Einstein–de Haas Effect, Phys. Rev. Lett. **112**, 085503 (2014).

[50] We note that this basis transformation is unity and as such maintains the completeness and closure relations of the eigendisplacements.

[51] M. Zacharias, H. Seiler, F. Caruso, D. Zahn, F. Giustino, P. C. Kelires, and R. Ernstorfer, Multiphonon diffuse scattering in solids from first principles: Application to layered crystals and two-dimensional materials, Phys. Rev. B **104**, 205109 (2021).

[52] B. Fultz and J. M. Howe, "Inelastic electron scattering and spectroscopy," in *Transmission Electron Microscopy and Diffractometry of Materials* (Springer, Berlin Heidelberg, 2008), pp. 163–221.

[53] M. Zacharias, H. Seiler, F. Caruso, D. Zahn, F. Giustino, P. C. Kelires, and R. Ernstorfer, Efficient First-Principles Methodology for the Calculation of the All-Phonon Inelastic Scattering in Solids, Phys. Rev. Lett. **127**, 207401 (2021).

[54] P. Debye, Interferenz von röntgenstrahlen und wärmebewegung, Ann. Phys. **348**, 49 (1913).

[55] I. Waller, Zur frage der einwirkung der wärmebewegung auf die interferenz von röntgenstrahlen, Z. Angew. Phys. **17**, 398 (1923).

[56] P. Giannozzi, S. Baroni, N. Bonini, M. Calandra, R. Car, C. Cavazzoni, D. Ceresoli, G. L. Chiarotti, M. Cococcioni, I. Dabo, A. D. Corso, S. de Gironcoli, S. Fabris, G. Fratesi, R. Gebauer, U. Gerstmann, C. Gougoussis, A. Kokalj, M. Lazzeri, L. Martin-Samos, N. Marzari, F. Mauri, R. Mazzarello, S. Paolini, A. Pasquarello, L. Paulatto, C. Sbraccia, S. Scandolo, G. Sclauzero, A. P. Seitsonen, A. Smogunov, P. Umari, and R. M. Wentzcovitch, QUANTUM ESPRESSO: A modular and open-source software project for quantum simulations of materials, J. Phys.: Condens. Matter **21**, 395502 (2009).

[57] P. Giannozzi, O. Andreussi, T. Brumme, O. Bunau, M. B. Nardelli, M. Calandra, R. Car, C. Cavazzoni, D. Ceresoli, M. Cococcioni, N. Colonna, I. Carnimeo, A. D. Corso, S. de Gironcoli, P. Delugas, R. A. DiStasio, A. Ferretti, A. Floris, G. Fratesi, G. Fugallo, R. Gebauer, U. Gerstmann, F. Giustino, T. Gorni, J. Jia, M. Kawamura, H.-Y. Ko, A. Kokalj, E. Küçükbenli, M. Lazzeri, M. Marsili, N. Marzari, F. Mauri, N. L. Nguyen, H.-V. Nguyen, A. O. de-la Roza, L. Paulatto, S. Poncé, D. Rocca, R. Sabatini, B. Santra, M. Schlipf, A. P. Seitsonen, A. Smogunov, I. Timrov, T. Thonhauser, P. Umari, N. Vast, X. Wu, and S. Baroni, Advanced capabilities for materials mod-elling with quantum ESPRESSO, J. Phys.: Condens. Matter **29**, 465901 (2017).

[58] J. Laval, Étude expérimentale de la diffusion des rayons x par les cristaux, Bull Minéral **62**, 137 (1939).

[59] M. Born, Theoretical investigations on the relation between crystal dynamics and x-ray scattering, Rep. Prog. Phys. **9**, 294 (1942).

[60] R. W. James, *The Optical Principles of the Diffraction of X-Rays* (G. Bell and Sons, London, 1948).

[61] N. Troullier and J. L. Martins, Efficient pseudopotentials for plane-wave calculations, Phys. Rev. B **43**, 1993 (1991).

[62] J. P. Perdew, K. Burke, and M. Ernzerhof, Generalized Gradient Approximation Made Simple, Phys. Rev. Lett. **77**, 3865 (1996).

[63] T. Sohier, M. Calandra, and F. Mauri, Density functional perturbation theory for gated two-dimensional heterostructures: Theoretical developments and application to flexural phonons in graphene, Phys. Rev. B **96**, 075448 (2017).

[64] This value is the average FWHM of the s^z distribution for the respective orbiting sublattices of the chiral modes. The results herein do not depend sensitively on the exact value chosen.